Available online at www.sciencedirect.com

ScienceDirect

Geochimica et Cosmochimica Acta 231 (2018) 50–63

Geochimica et Cosmochimica Acta

www.elsevier.com/locate/gca

Manganese and iron geochemistry in sediments underlying the redox-stratified Fayetteville Green Lake

Elizabeth M. Herndon [a,*], Jeff R. Havig [b,1], David M. Singer [a], Michael L. McCormick [c], Lee R. Kump [d]

[a] Department of Geology, 221 McGilvrey Hall, Kent State University, Kent, OH 44242, USA
[b] Department of Geology, University of Cincinnati, 500 Geology-Physics Building, Cincinnati, OH 45221, USA
[c] Biology, Hamilton College, 198 College Hill Road, Clinton, NY 13323, USA
[d] Department of Geosciences, Pennsylvania State University, University Park, PA 16802, USA

Received 26 June 2017; accepted in revised form 11 April 2018; Available online 17 April 2018

Abstract

Manganese and iron are redox-sensitive elements that yield clues about biogeochemistry and redox conditions both in modern environments and in the geologic past. Here, we investigated Mn and Fe-bearing minerals preserved in basin sediments underlying Fayetteville Green Lake, a redox-stratified lake that serves as a geochemical analogue for Paleoproterozoic oceans. Synchrotron-source microprobe techniques (μXRF, μXANES, and μXRD) and bulk geochemical analyses were used to examine the microscale distribution and speciation of Mn, Fe, and S as a function of depth in the top 48 cm of anoxic lake sediments. Manganese was primarily associated with calcite grains as a manganese-rich carbonate that precipitated in the chemocline of the water column and settled through the euxinic basin to collect in lake sediments. Iron was preserved in framboidal iron sulfides that precipitated in euxinic bottom waters and underwent transformation to pyrite and marcasite in the sediments. Previous studies attribute the formation of manganese-rich carbonates to the diagenetic alteration of manganese oxides deposited in basins underlying oxygenated water. Our study challenges this paradigm by providing evidence that Mn-bearing carbonates form in the water column and accumulate in sediments below anoxic waters. Consequently, manganoan carbonates preserved in the rock record do not necessarily denote the presence of oxygenated bottom waters in ocean basins.

Keywords: Manganese; Iron; Redox; Spectroscopy

1. INTRODUCTION

Redox-sensitive elements such as Mn and Fe record paleoredox conditions and have been used to evaluate the redox state of the oceans throughout geologic time (Arnold et al., 2004; Rouxel et al., 2005; Scott et al., 2008; Planavsky et al., 2011; Poulton and Canfield, 2011; Johnson et al., 2013; Reinhard et al., 2013). Studies indicate that Earth's oceans were locally to globally stratified for over half of Earth's history, with transient oxic surface waters overlying anoxic to euxinic deep waters throughout the Proterozoic and even during periods in the Archaean and Phanerozoic (Kump et al., 2005; Meyer and Kump, 2008; Severmann et al., 2008; Planavsky et al., 2011; Poulton and Canfield, 2011). Precipitation of known Fe and Mn ores predominantly occurred in the Neoarchean (>50% of known iron ores (Bekker et al., 2010)), during the lead up to the Great Oxidation Event, and during the Paleoproterozoic period of rapid accumulation of

* Corresponding author.
E-mail address: eherndo1@kent.edu (E.M. Herndon).
[1] Now at Department of Earth Sciences, University of Minnesota, 150 Tate Hall, Minneapolis, MN 55455, USA.

https://doi.org/10.1016/j.gca.2018.04.013
0016-7037/

atmospheric O_2 (>50% of manganese ores (Maynard, 2010)). Previous studies attribute the formation of manganese carbonate ores to diagenesis of manganese oxides in sediments underlying permanently or transiently oxygenated basins (Calvert and Pedersen, 1996; Huckriede and Meischner, 1996; Johnson et al., 2013, 2016b). Here, we evaluated the geochemistry of Mn and Fe in sediments underlying a modern, redox-stratified lake in order to constrain the mechanisms driving the formation of Mn and Fe bearing minerals for events recorded in the rock record.

Fayetteville Green Lake (FGL) near Fayetteville, N.Y., United States was the first meromictic lake to be described in North America (Eggleton, 1931). The upper oxic mixolimnion of the FGL water column is separated from the lower euxinic monimolimnion by a chemocline that exhibits a dramatic shift in oxidation-reduction potential at 20.5 m depth (Havig et al., 2015) (Fig. 1). The oxic zone experiences seasonal "whiting" events where the exponential growth of cyanobacteria facilitates calcite precipitation by increasing alkalinity and providing mineral nucleation sites (Thompson et al., 1997). Sulfate-rich groundwater discharges from the gypsum-bearing Vernon Shale into the chemocline, and microbial sulfate-reduction drives sulfide generation which supports dense populations of anoxygenic phototrophs and generates persistently euxinic bottom waters. Sulfate concentrations in FGL (9.5–15.6 mM) (Havig et al., 2015) are similar to values estimated for Proterozoic Oceans following the Great Oxidation Event as continental sulfides underwent rapid oxidative weathering, releasing sulfate into the oceans (Planavsky et al., 2012).

Although microorganisms are thought to drive precipitation of Mn and Fe in the water column, the chemical species of Mn and Fe formed at the redox boundary as a result of microbial activity remain unclear. Particulate Fe and Mn oxides that are formed by microbial processes or input to FGL through watershed runoff undergo reductive dissolution as they settle through the chemocline. Total dissolved Mn and Fe concentrations are relatively low in the slightly alkaline oxic zone (<0.03 μmol L^{-1}) but increase orders of magnitude in the oxygen minimum zone (Havig et al., 2015). The processes that transport these metals through the water column and preserve them in lake sediments remain unknown. Sediment characterization is required to link the cycling and precipitation of Mn- and Fe-bearing minerals in the water column to deposition in the sediments.

We explore the hypothesis that biogenic calcite produced seasonally in the oxic zone provides nucleation sites for manganoan carbonate precipitation (Franklin and Morse, 1983; Mucci, 1988; Bottcher, 1998) and drives removal of Mn^{2+} from the water column (Havig et al., 2015). FGL sediments contain carbonates that are sourced primarily from biogenic precipitation in the water column rather than in the sediments (Havig et al., 2017; Fig. S1). Removal of Fe from the water column has been proposed to be mediated by precipitation of the Fe-Mo-S mineral $FeMo_{0.6}S_{2.8}$ (e.g., Helz et al., 2011) or by the mixed-valence mineral greigite (Fe_3S_4) (Havig et al., 2015).

2. METHODS

2.1. Water and sediment geochemical analyses

Water and sediment samples were collected from the center of Fayetteville Green Lake in the deep basin (Fig. 1). Optical dissolved oxygen (D.O.), pH, and oxidation-reduction potential (ORP) were determined *in situ* with a calibrated YSI 6600 multi-parameter sonde probe (YSI Incorporated, Yellow Springs, OH, USA). Water column samples were collected as described previously (Havig et al., 2015) using a high depth resolution full water column instantaneous sampler (McCormick et al., 2014), with water samples processed immediately after collection at Hamilton College. Total sulfide ($\Sigma S^{2-} = H_2S + HS^- + S^{2-}$) concentrations were determined from 1 mL sample aliquots dispensed into 2 mL screw top microcentrifuge tubes pre-filled with 0.5 mL of 20% w/w zinc acetate solution. Samples were then vortexed for 5 s and stored at 4 °C in the dark until analysis. Sulfide was determined colorimetrically (Cline, 1969). Samples for trace element analysis were filtered through a 25 mm diameter 0.22 μm polyethersulfone syringe filter (VWR International) into acid-washed (10% trace element grade HNO_3 soak for three days, triple rinsed with 18.2 MΩ/cm deionized water) 15 mL falcon tubes pre-doped with concentrated OmniTrace Ultra HNO_3 (EMD Millipore Corp., Merck KGaA, Darmstadt, Germany).

Sediment cores were collected to a depth of ~48 cm using 2-inch diameter gravity corers fitted with ~50 cm long polycarbonate liners. One sediment core was kept on ice after collection and processed immediately after sampling for sectioning and pore water recovery. Sediment subsamples were collected by extrusion and sectioning into a N_2-filled and positive pressure glove box. Pore water was recovered by centrifugation of sediments in gas tight Oak Ridge tubes (5000 RPM at 4 °C for 10 min) with a N_2 headspace, and supernatant water was drawn into a syringe and filtered as described above. Two portions of each dried sediment section depth were collected for bulk Mn and Fe determinations. One of the portions was acidified with 1 M HCl for 24 h prior to centrifugation at 3000 RPM for five minutes, and the resulting supernatant was poured off to completely remove the acid-soluble fraction. The acidified sediments were then rinsed three times with 18.2 MΩ cm^{-1} deionized water, centrifuged, and the supernatant was discarded to remove all residual HCl. Acidified samples were then dried and reground via mortar and pestle to assure homogenization. Non-acidified and acidified sediments were digested in a concentrated HNO_3-HCl solution (following EPA method 3051) using a CEM MARS Express microwave digestion system (CEM Corporation, North Carolina, USA) by the STAR Lab at the Ohio State University to bring the sediments into solution for Mn and Fe determination. Iron and manganese were analyzed via a Teledyne Leeman Labs Prodigy Dual view Inductively Coupled Plasma Optical Emission Spectrometer (ICP-OES) (Teledyne Leeman Labs, Hudson, New Hampshire,

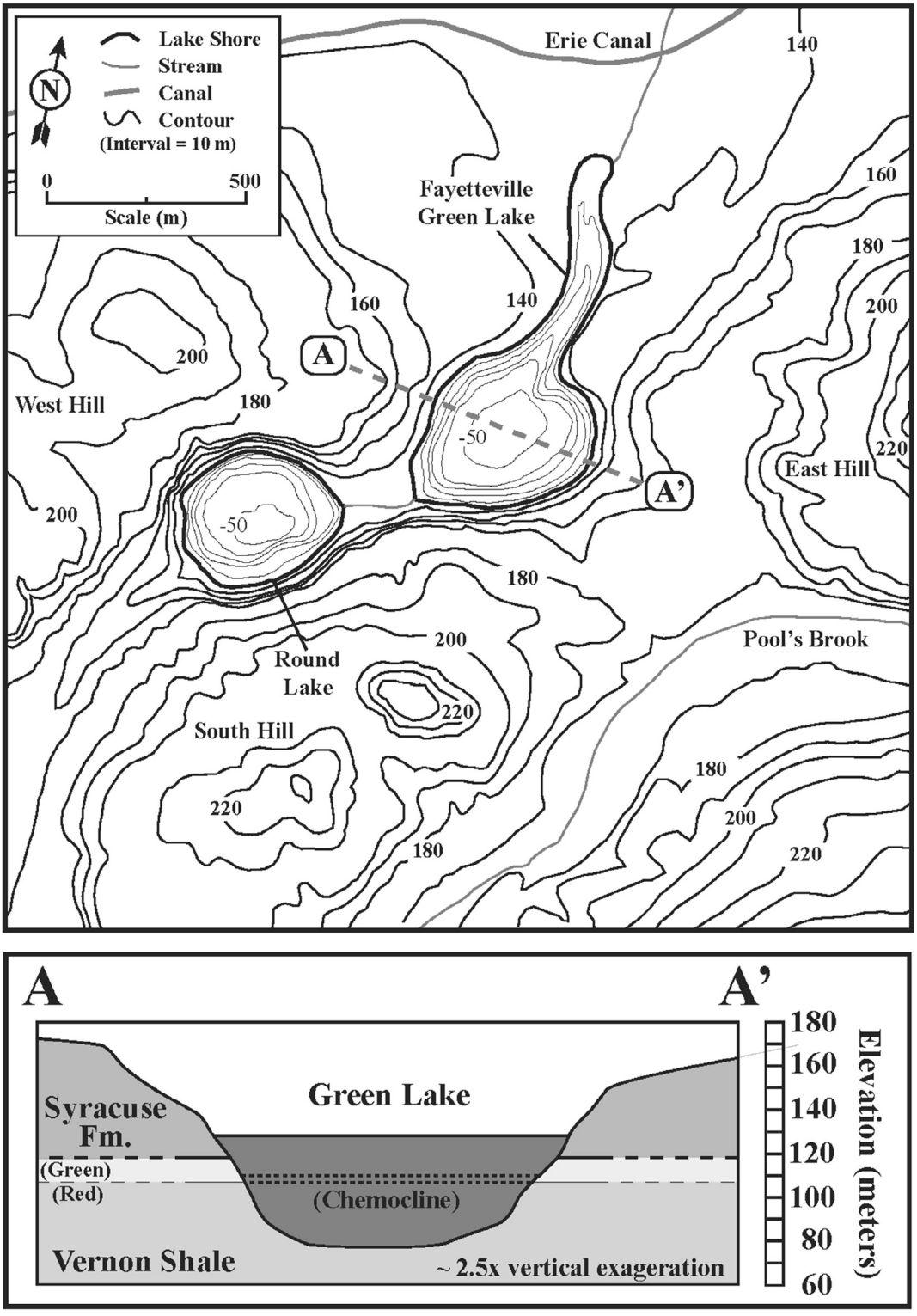

Fig. 1. (top panel) Topographic map of Fayetteville Green Lake (FGL) and surrounding area, located outside of Fayetteville, New York, USA. Contour intervals indicate 10 m elevation change. (bottom panel) FGL cross-section from points A to A′ shown in panel (a), showing the elevation of the lake and its stratified layers (e.g., chemocline) and bordering lithological units. Groundwater discharge of high sulfate from the Vernon Green Shale supports microbial sulfate reduction which maintains euxinic conditions within the lake.

USA) by the STAR Lab. Detection limits were reported as 18.2 nmol L^{-1} for Mn and 17.9 nmol L^{-1} for Fe.

Saturation indices were calculated from the 2013 geochemical data due to completeness of the dataset, as reported in (Havig et al., 2015). In short, saturation indices for calcite ($CaCO_3$), rhodochrosite ($MnCO_3$), and kutnohorite ($CaMn(CO_3)_2$) were calculated using ionic strength to determine activity coefficients (see Appendix A). Ionic strengths were determined using major anion and cation concentrations. Concentrations of CO_3^{2-} and HCO_3^- were determined from DIC concentrations via CO2Sys_v2.1 developed by Pierrot et al. (2006) using the parameters outlined by Havig et al. (2017). K_{sp} values were obtained from Jensen et al. (2002) for calcite and rhodochrosite and from Mucci (2004) for kutnohorite.

2.2. Sediment thin section preparation

A sediment core (48 cm in length) was collected from Fayetteville Green Lake in July 2015 using a gravity corer, then immediately frozen on dry ice and kept frozen during shipment and storage. The core was subsequently transported frozen into a Coy anaerobic chamber with ~98% N_2 and 2% H_2 atmosphere, then removed from its plastic liner for processing. A multipurpose oscillating power tool was used to segment the core into ~5 cm depth increments which were thawed and dried at room temperature in the anaerobic chamber. Dried sediments were lightly ground into a powder with a mortar and pestle, then stored in glass vials, sealed in an oxygen-free transport (AnaeroPak), and shipped to Spectrum Petrographics (Vancouver, WA) for thin section preparation. Sediments were embedded in epoxy immediately upon removal from their vials, prepared as standard (30 μm thick) thin sections, and mounted on quartz glass slides.

2.3. Spectroscopic characterization

Sediment thin sections ($n = 9$) were initially characterized for grain size, morphology, and chemistry using a Hitachi Benchtop TM3030 scanning electron microscope equipped with Quantax70 energy dispersive X-ray spectrometry (SEM-EDS). Element maps were collected at 15 keV and element stoichiometry was quantified for areas of interest. Subsequent X-ray microprobe analysis was conducted at GSECARS beamline 13-ID-E at the Advanced Photon Source (Argonne National Laboratory). Micro-X-ray fluorescence (μXRF) maps (800 × 800 μm) were generated with a 2 × 2 μm focused beam at 7100 eV to evaluate spatial association of Fe and Mn with other elements of interest (e.g., Ca), and at 2490 eV to determine the spatial distribution of S redox species and spatial associations with Si and Fe. Micro-XRF maps were further used to identify regions of interest for micro-X-ray near edge structure (μXANES) spectroscopy and micro-X-ray diffraction (μXRD). XANES spectra were collected from −50 to +550 eV around the Mn K-edge ($E_0 = 6539$ eV), Fe K-edge ($E_0 = 7112$ eV), and S K-edge ($E_0 = 2472$ eV). The spatial distribution of S redox species, defined operationally as reduced (S_{RED}), zero valent (S^0), and oxidized (S_{OX}), was constructed based on maps collected at 2471 eV, 2473 eV, 2478 eV, 2482 eV, and 2490 eV. Definition of S redox species was supported by μXANES spectra at selected spots. Micro-XRD patterns were collected on selected areas in transmission geometry using a CCD area detector with the incident beam energy set at 18 keV (0.6888 Å).

Microprobe data analyses were conducted in Larch (Newville, 2013). Micro-XRF maps were visualized using DataViewer software. Micro-XANES spectra were calibrated to a zero-valent Fe foil (E0 = 7110.7 eV) (Kraft et al., 1996) and compared to reference spectra for Mn (Manceau et al., 2012; Johnson et al., 2016a, 2016b) and Fe, reported by the Advanced Light Source at Berkeley National Laboratory, using Athena software (Demeter v.0.9.25). Reference spectra for Mn include the Mn(II)-bearing carbonates rhodochrosite ($MnCO_3$), kutnohorite ($CaMn(CO_3)_2$), and manganoan calcite, the Mn-oxide minerals MnO, Mn_3O_4, Mn_2O_3, and pyrolusite (MnO_2), the Mn sulfide minerals alabandite and rambergite (both MnS; Lenz et al., 2014), and braunite ($Mn_6^{III}Mn^{II}O_8SiO_4$), which serves as a proxy for silicate minerals. Reference spectra for Fe include siderite ($FeCO_3$), pyrite (FeS_2), mackinawite (FeS), greigite (Fe_3S_4) (Noël et al., 2014), magnetite (Fe_3O_4), and ferrihydrite (ferric oxyhydroxide) (Table S1). X-ray diffraction images were processed with DIOPTAS software (Prescher and Prakapenka, 2015) using CeO_2 as a standard for geometrical calibration. Mineral phase identification was performed using JADE 6.5 (Materials Data Inc., Livermore, CA).

3. RESULTS

3.1. Water and sediment geochemistry

The mixolimnion layer of the lake extended from the surface to 15 m depth and was characterized by high concentrations of dissolved oxygen (>250 μmol L^{-1}), positive oxidation-reduction potentials, and low concentrations of dissolved Mn and Fe (<0.1 μmol L^{-1}) (Fig. 2). Dissolved oxygen concentrations decreased to near zero through the chemocline, coincident with increases in concentrations of dissolved Mn and Fe that peaked at 61 μmol L^{-1} Mn and 3.2 μmol L^{-1} Fe at ~20 m depth. In the lower monimolimnion, dissolved oxygen remained negligible, while concentrations of dissolved sulfide species increased from below detection to nearly 2 mmol L^{-1}. Concentrations of dissolved Mn decreased to <4 μmol L^{-1} through the euxinic bottom waters while concentrations of dissolved Fe decreased to ~0.1 μmol L^{-1}. Depth profiles of dissolved constituents were consistent amongst sampling dates.

The mixolimnion was oversaturated with respect to calcite but undersaturated with respect to the Mn-bearing carbonates rhodochrosite and kutnohorite (Fig. 2). Conversely, the chemocline was undersaturated with respect to calcite and oversaturated with respect to rhodochrosite and kutnohorite. Saturation indices for calcite remained negative throughout the monimolimnion, while saturation indices for rhodochrosite and kutnohorite were positive or near zero.

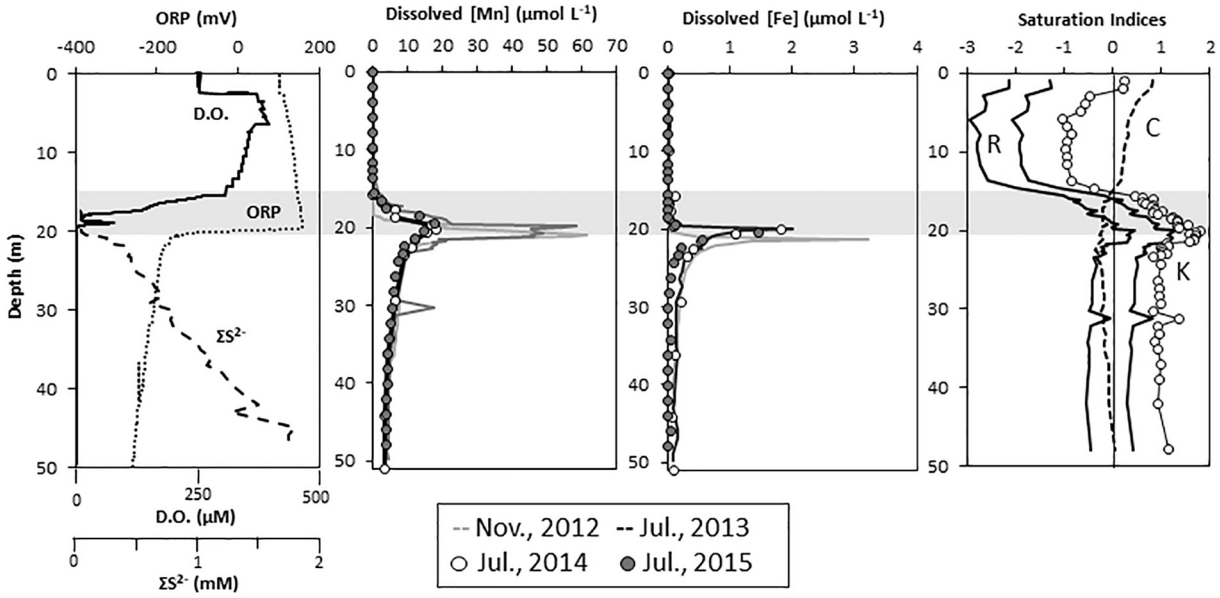

Fig. 2. Fayetteville Green Lake water column chemistry. Horizontal shaded bar indicates the depth interval of the chemocline. Dissolved oxygen (DO; μM) and oxidation-reduction potential (ORP; V) are high in the slightly alkaline (pH ~ 7.5 to 8) mixolimnion and decline through the chemocline, while total concentrations of dissolved sulfide species (ΣS^{2-}; mM) increase steadily below the chemocline into the circumneutral (pH ~ 6.5–7) bottom waters (Havig et al., 2015). Concentrations of dissolved Mn (μM) and Fe (μM) vary by orders of magnitude and peak near the bottom of the chemocline. Saturation indices as a function of depth are shown for rhodochrosite (R; solid black lines), kutnohorite (K; open circles), and calcite (C; dashed grey line). SI calculations are summarized in Appendix A.

Concentrations of dissolved Mn and Fe decreased with depth in the sediments (Fig. 3). Mn concentrations in sediment pore waters (<2 μmol L^{-1}) were lower than in overlying anoxic bottom waters (~4–100 μmol L^{-1}). In contrast, dissolved Fe concentrations were higher in the sediments (2.8–9.0 μmol L^{-1}; Fig. 3 and Table S3) than in lake bottom waters (<2 μmol L^{-1}) (Fig. 2 and Table S2).

Sediments were dominated by carbonates at all depths, but the carbonate fraction increased from ~70 wt.% $CaCO_3$ above 20 cm depth to ~90 wt.% $CaCO_3$ below 30 cm depth (Fig. 3; Table S4). Total concentrations of solid-phase Mn and Fe peaked at 20 cm in the sediments and were low in deep sediments relative to shallow sediments. Acid-soluble Mn comprised up to ~85% of total sediment Mn and followed the same trend as total carbonates. Acid-soluble Fe exhibited a similar trend but comprised <50% of sediment iron.

3.2. Microscale sediment geochemistry

Lake sediments were primarily composed of rhombohedral calcite ($CaCO_3$) grains intermixed with diatoms, organic material, aluminosilicates, and iron sulfides (Figs. 3 and 4). Calcite grains were sparse and mostly small (<10 μm long axis) in the top 5 cm of sediment but increased in size (up to 20 μm long axis) and abundance with depth. Manganese concentrations in individual carbonate grains could not be quantified because Mn was below detection of the EDS. Diatom frustules, composed of Si and O, were most abundant at the sediment surface (0–5 cm) (Fig. 4). Aluminosilicate minerals were present in stacked layers and irregular grains. Low-contrast materials that contained minimal quantities of rock-derived elements were inferred to be organic matter from decomposing plant material. Elongate crystals containing Ca and S, which we infer to be gypsum as previously identified (Thompson and Ferris, 1990), were only observed in the surface sediment (data not shown).

Manganese was co-located with Ca throughout the sediment core (Figs. 5, S2 and S3), often forming discernable Mn-rich rims around Ca-bearing grains (e.g., Fig. 5A). Mn K-edge μXANES spectra obtained on Ca-rich grains were similar to carbonate minerals such as Mn-bearing calcite ($MnCaCO_3$), rhodochrosite ($MnCO_3$) and kutnohorite ($CaMn(CO_3)_2$) (Fig. 5B) (Johnson et al., 2016b), and rhodochrosite peaks were identified by μXRD (Figs. 5D, S7 and S8). Manganese was also present in Fe-rich grains that did not contain appreciable Ca (Fig. 5A) and were identified as mixtures of Fe and Mn sulfides. Mn K-edge μXANES in the Fe-rich grains (Fig. 5B) exhibited a similar spectral shape to Fe K-edge XANES for iron sulfides (Fig. 5C), suggesting the presence of either a MnS phase or Mn-substituted iron sulfide. Although these XANES spectra were distinct from pure MnS phases (Lenz et al., 2014) (Fig. S2), rambergite (γ-MnS) was identified by μXRD (Fig. 5D). No reference spectrum for Mn-substituted iron sulfide was available for direct comparison.

Spherical particles and fragments of spherical particles ranging from approximately 50 to 400 μm diameter were observed at all depths. Mn μXANES in these and other grains, labeled "deposited particles", were dissimilar from carbonate or sulfide species but similar to mixed-valence Mn (II/III)-bearing minerals such as braunite

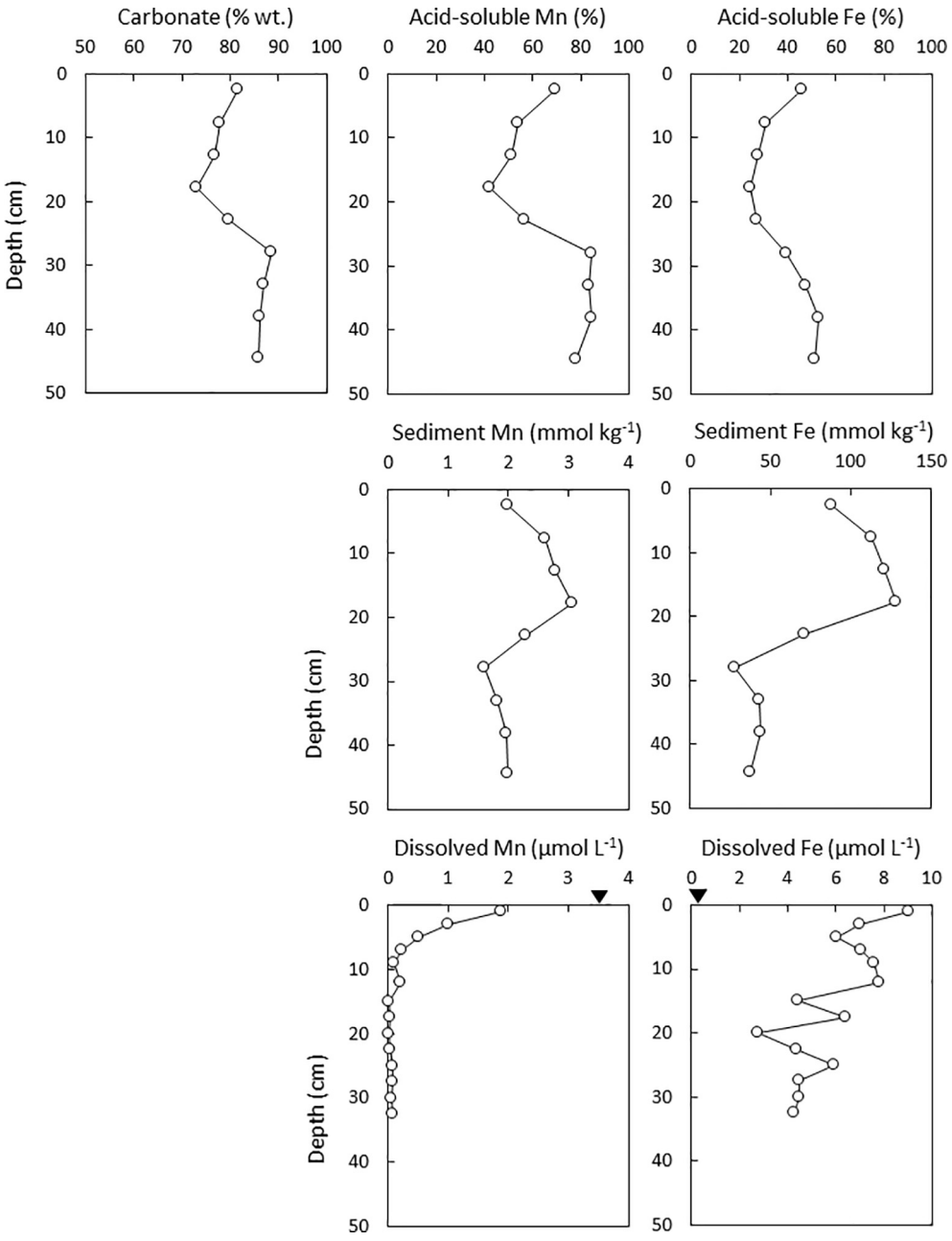

Fig. 3. Concentrations of solid-phase and dissolved constituents versus depth in the top 48 cm of lake sediments. Carbonate concentration (wt.%) is equal to the weight percent of bulk sediment comprised of carbonate minerals. Acid-soluble Mn and Fe (%) is the percent of each element in the bulk sediment that is acid-soluble. Sediment Mn and Fe (mmol kg^{-1}) is the total concentration of each element in the bulk sediment. Dissolved Mn and Fe (µmol L^{-1}) is the filterable concentration of the element in sediment pore water, and the arrow on each graph indicates the concentration of that element in the deepest sampled lake water. Concentrations and sampled depth increments are reported in Tables S3 and S4.

($Mn_6^{III}Mn^{II}O_8SiO_4$) and Mn_3O_4 (Fig. 5B and S2). Specifically, these grains contained Mn with an average oxidation state of 2.7 ± 0.2, which was consistent with mixed-valence Mn(II/III) minerals but inconsistent with Mn(III/IV) oxides. Absorption edges and white line features for all spectra for deposited particles were shifted to lower energies than Mn(IV) oxide standards. The potential for Mn in these grains to be present in detrital silicates is supported by µXRD results that identify a mix of silicates (albite, orthoclase, quartz, muscovite) (Fig. 5D), and by the presence of Si in these features (Fig. 6). Here, we use the term deposited particles to refer to non-carbonate and non-sulfide material that originates either in the water column or from outside the lake and subsequently settles through the water column and accumulates in the sediments. In contrast, authigenic material is formed in the sediments.

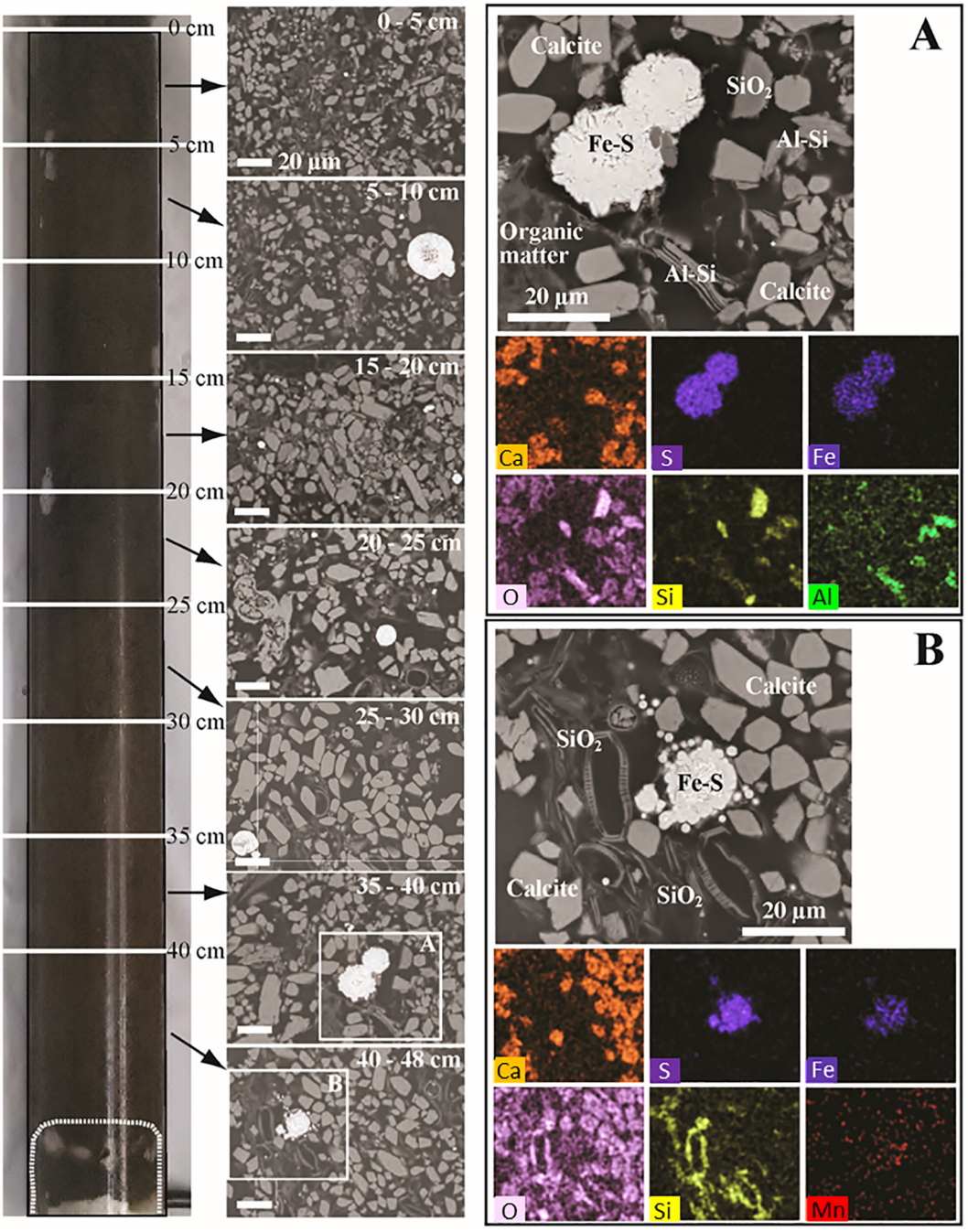

Fig. 4. Scanning electron microscopy images of FGL sediment collected from 0 to 48 cm depth in 5 to 8 cm increments. Inset boxes in the 35–40 cm and 40–48 cm images correspond to areas shown in panels (A) and (B). Major sediment constituents are labeled in (A) and (B), including calcite, iron sulfides (Fe-S), diatoms and quartz minerals (SiO_2), aluminosilicate minerals (Al-Si) and organic matter. Corresponding maps obtained by SEM-EDS show the spatial distribution of major elements (Ca, S, Fe, O, Si, Al) used to support constituent identification. Manganese concentrations were below detection of EDS at the scales analyzed. Scale bars in all maps are 20 µm.

Iron was present in aluminosilicates and in sulfide minerals such as mackinawite (FeS), greigite (Fe_3S_4), and pyrite and marcasite (FeS_2). Iron sulfides occurred primarily as framboids ranging from <5 µm to 100 µm in diameter, with a median diameter of 13 µm for grains larger than 5 µm, as measured by SEM (Figs. 4 and 7). A subset of framboids exhibited overgrowth features consistent with diagenetic alteration (Wilkin and Barnes, 1997; Suits and Wilkin, 1998) (Fig. 7). The average S content of analyzed iron sulfides was 61 ± 13 at.% (± std. dev.) (n = 46). Of these grains, 46% had a stoichiometry corresponding to pyrite or marcasite (66 ± 3 at.% S), 24% corresponding to greigite (57 ± 3 at.% S), and 13% had a stoichiometry intermediate between FeS_2 and Fe_3S_4, consistent with a mixture of multiple phases. Other grains contained <54 at.% S, indicating either the presence of mackinawite (FeS) or contribution of

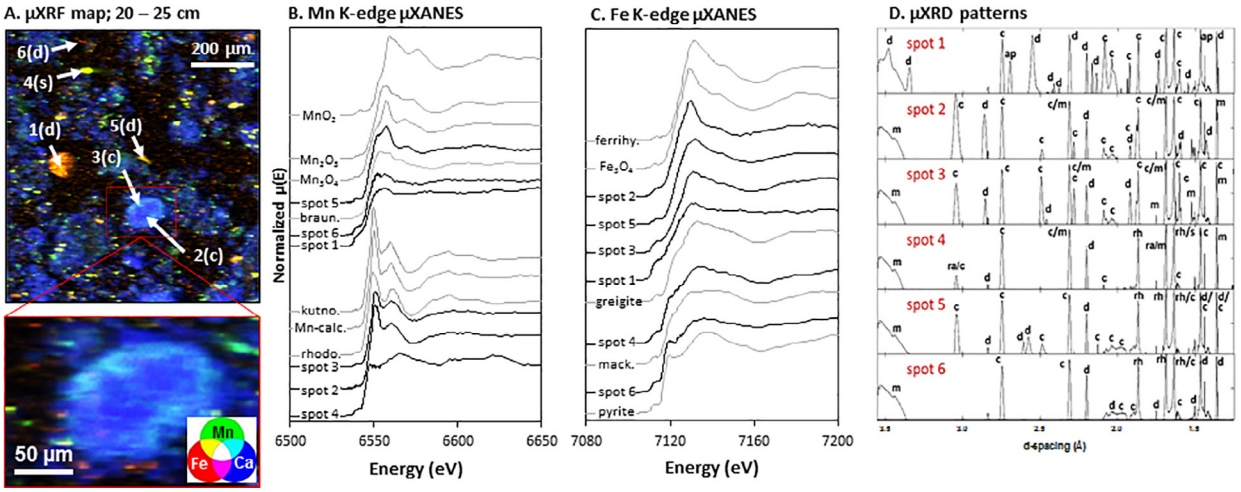

Fig. 5. (A) Micro-X-ray fluorescence map of Mn (green), Fe (red), and Ca (blue) in FGL sediment collected from 20 to 25 cm depth. Other colors indicate overlapping elements, as shown in the color wheel. Arrows indicate spots identified as carbonate (c), sulfide (s), or other deposited mineral (d) grains. One carbonate grain with a Mn-rich rim is expanded in the lower image. (B) Mn K-edge µXANES spectra from the spots indicated in the µXRF map. Sample spectra are shown as solid lines and reference spectra are shown as dashed lines. Reference spectra include kutnohorite, rhodochrosite, Mn_3O_4, and braunite. (C) Fe K-edge µXANES spectra from the spots indicated in panel (A). Reference spectra include ferrihydrite, magnetite (Fe_3O_4), greigite, mackinawite (mack.), and pyrite. (D) Diffraction peaks obtained from spots in panel (A) indicate the presence of detrital silicates (d = muscovite + orthoclase + albite), calcium carbonates (c = calcite + shortite), rhodochrosite (rh), marcasite (m), rambergite (ra), and fluorapatite (ap). Individual diffraction patterns are provided in Figs. S7 and S8. (For interpretation of the references to colour in this figure legend, the reader is referred to the web version of this article.)

excess Fe from a non-sulfide mineral such as an iron oxide. No grains had a stoichiometry consistent with the proposed $FeMo_{0.6}S_{2.8}$ mineral (Helz et al., 2011).

Iron was primarily associated with S-rich spots in µXRF maps (Fig. 6) and exhibited µXANES spectra consistent with either iron (II) sulfide or magnetite and greigite standards (Fig. S4). Linear combination fits to the Fe (II) XANES spectra were most consistent with pyrite and mackinawite (Table S5). All remaining spectra had adsorption edges that were consistent with magnetite and greigite (average Fe valence = +2.67) but shifted to lower energies than ferrihydrite (average Fe valence = +3.0). It was not possible to differentiate further between these phases with our data, but stoichiometry results from SEM-EDS analysis suggest a high contribution of greigite. No Fe spectra were consistent with iron carbonate, e.g., siderite ($FeCO_3$). Marcasite was the only Fe sulfide identified by µXRD (Figs. 5D, S7 and S8), likely due to poor crystallinity of the other sulfide phases. Sulfur K-edge XANES revealed reduced sulfur (S^{2-}) in Fe-rich spots indicative of sulfide minerals, zero-valent sulfur (S^0) associated with apparent structures of biological origin (e.g., Fig. 6f), and oxidized sulfur (S^{6+}) in diffusely distributed or aggregated patches of sulfate (Figs. 6 and S5).

4. DISCUSSION

4.1. Manganese geochemistry

The carbonate fraction of the sediments and the size of individual calcite grains decreased from old deep sediments to young shallow sediments (Fig. 3; Table S4), likely resulting from changes in environmental conditions and sedimentation that occurred during the transition from an undisturbed to a human-impacted watershed. Anthropogenic acidification has inhibited rates of calcite precipitation in the post-1850 industrial age, leading to smaller calcite grains in shallow sediments (Havig et al., 2017). Additionally, the onset of European settlement marked a sevenfold increase in sediment accumulation rates in Green Lake due to local deforestation that increased sediment runoff (Hilfinger et al., 2001). Increased inputs of silicate minerals from sediment runoff would explain decreases in the carbonate fraction. The increase in total Mn and Fe but decrease in acid-soluble Mn and Fe above 20 cm points supports an increased input of detrital, acid-insoluble aluminosilicates from surface runoff (Hilfinger et al., 2001).

Acid-soluble Mn, inferred to be hosted in carbonates, comprised 40–85% of sediment Mn and followed the same trend as total carbonates (Fig. 3; Table S4). Thus, Mn in the sediments appears to be dominated by the carbonate fraction, as observed for other anoxic systems (e.g., Kiratli and Ergin, 1996). The extent to which Mn-S phases contribute to acid-soluble Mn is unclear; however, acid-soluble Mn (%) is more strongly correlated with sediment carbonates (wt.%) (R^2 = 0.97) than with acid-soluble Fe (%) (R^2 = 0.79). Spectroscopic analyses confirmed that Mn-bearing carbonates were associated with calcite grains (Figs. 5 and S1). Previous studies indicate that sediment carbonates at FGL are isotopically similar ($\delta^{13}C$ = −4.3‰) to the biogenic carbonates that precipitate in oxic surface waters ($\delta^{13}C$ = −5.5‰), but dissimilar from dissolved inorganic carbon that is released from decomposing organic matter in sediment pore waters ($\delta^{13}C$ = −19.4 to −25.2‰) (Takahashi et al., 1968; Fry, 1986; Thompson et al., 1997; Havig et al., 2017). Consequently, sediment

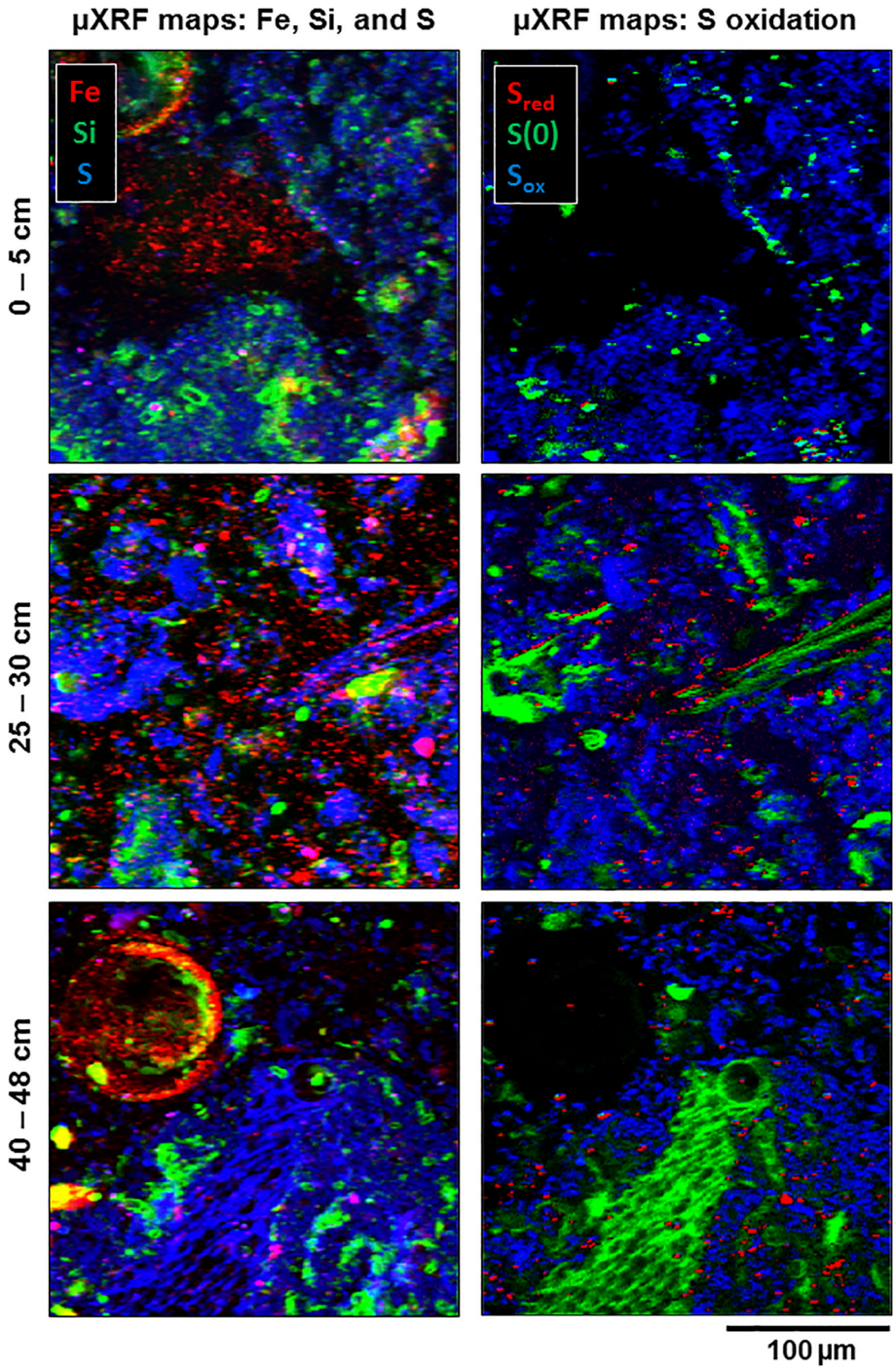

Fig. 6. Left panels show three element (Fe, Si, and S) micro-X-ray fluorescence maps acquired at low energy. Right panels show corresponding S redox maps for reduced (S_{red}; S^{2-}), zero-valent (S^0), and oxidized sulfur (S_{ox}; S^{6+}). Scale bar is the same for all panels. Note, these maps do not correspond to the same areas as the maps shown in Fig. 5.

carbonates must derive from grains that form in the oxic zone and settle through the water column rather than authigenic precipitates that form during decomposition of sedimentary organic matter. We propose that calcite that precipitates in the oxic zone acts as a nucleation site for Mn^{2+} to precipitate the observed manganoan carbonate phase as it settles through the chemocline (Franklin and Morse, 1983; Mucci, 1988; Pingitore et al., 1988; Bottcher, 1998). Precipitation of distinct $MnCO_3$ phases has been hypothesized to similarly remove Mn from the water column of the high-salinity, redox-stratified Orca Basin (Van Cappellen et al., 1998). The chemocline and monimolimnion were undersaturated with respect to calcite but oversaturated with respect to rhodochrosite and

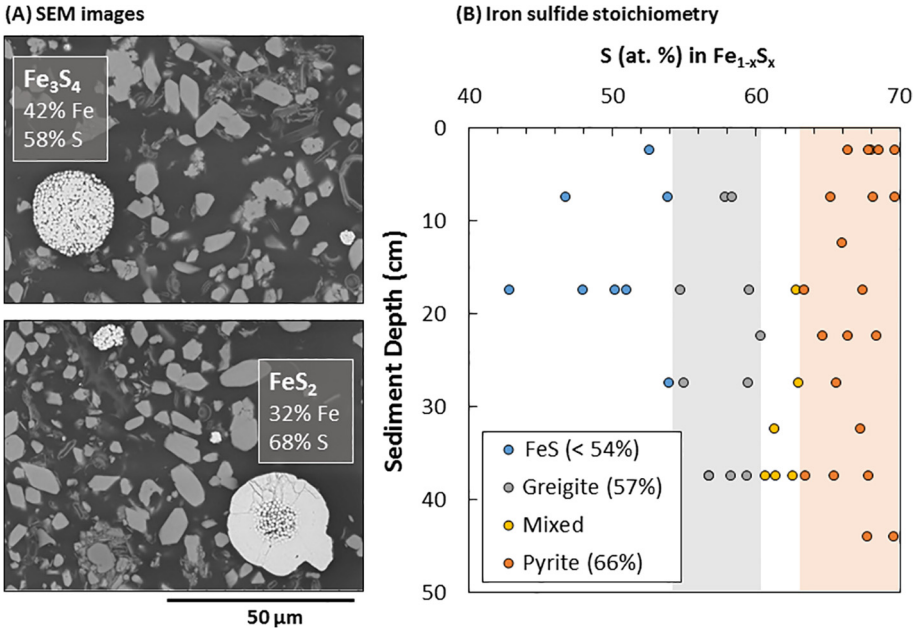

Fig. 7. (A) Scanning electron microscopy images of iron sulfide framboids with stoichiometry similar to either greigite (Fe_3S_4) or pyrite and marcasite (FeS_2). Note that the FeS_2 framboid exhibits significant overgrowth consistent with diagenesis (Suits and Wilkins, 1998). Fe:S stoichiometry was quantified by energy dispersive X-ray spectroscopy. (B) Sulfur content (at.%) of all examined iron sulfide minerals as a function of sediment depth. Shaded vertical bars indicate grain stoichiometries consistent with either greigite (grey) or pyrite/marcasite (orange) with ±3% error. These regions were used to classify individual grains as a FeS_2 phase (66 ± 3 at.% S), greigite (57 ± 3 at.% S), an FeS such as mackinawite (<54 at.% S), or a mixture of FeS_2 and greigite phases (60–63 at.% S).

kutnohorite (Fig. 2), reinforcing the likelihood for these manganoan carbonate phases to form in the water column. $MnCO_3$ co-precipitation with $CaCO_3$ as "pseudokutnohorite," an intermediate $MnCO_3$-$CaCO_3$ solid-solution, is favored when high concentrations of dissolved Mn^{2+} are coupled with low concentrations of Mg^{2+} and slow precipitation rates (Franklin and Morse, 1983; Mucci, 1988; Pingitore et al., 1988; Bottcher, 1998). The formation of Mn-rich rims may preserve calcite grains from dissolution as they settle through the euxinic bottom waters where saturation indices for calcite are below zero.

It is less likely that the observed Mn-carbonate phase precipitated authigenically in the lake sediments. First, dissolved Mn concentrations decreased with increasing depth in the monimolimnion and were over an order of magnitude lower in sediment pore waters (<2 µmol L^{-1}) than in the euxinic zone (~60 µmol L^{-1}) (Figs. 2 and 3). This decline in dissolved Mn^{2+} indicates removal from the water column, presumably due to precipitation as carbonates, and lowers the saturation indices for these phases to near zero in the sediments. Decreasing Mn^{2+} in sediment pore waters with depth may represent either relatively minor substitution of Mn into carbonate phases without authigenic carbonate precipitation, or incorporation of Mn into sulfide minerals (Suess, 1978; Bottcher and Huckriede, 1997).

Manganese substitution into Fe sulfide minerals and/or formation of a co-occurring but independent sulfide phase is supported by the presence of Mn in non-carbonate, Fe-rich grains (Huerta-Diaz and Morse, 1992; Morse and Luther, 1999). The Mn XANES spectra obtained from these grains were similar to the Mn sulfide component in Baltic Sea sediments, which were attributed to Mn that substituted into Fe sulfides such as pyrite and mackinawite (Lenz et al., 2014). However, detection of rambergite (γ-MnS) by µXRD indicates that Mn sulfides were present in addition to Fe sulfide minerals in our study. Manganese sulfides such as rambergite have been observed in deep anoxic basins of the Baltic Sea (Suess, 1978; Bottcher and Huckriede, 1997), and "oxidizable Mn" which includes Mn sulfides was found to comprise variable portions of Mn in Black Sea sediments (Kiratli and Ergin, 1996). It was not possible to fully differentiate between Mn in Mn-sulfides versus Mn-bearing Fe-sulfides given their close spatial associations, and more investigation is needed to definitively assign a mineral phase for sulfidic Mn. Regardless, these sulfides may serve as sinks that scavenge dissolved Mn in the top 10 cm of sediment pore waters (Fig. 3).

Spherical particles likely consisted of micron-sized clays and other minerals that were dispersed into a spherical shape by bubble formation in the epoxy during thin section preparation (Fig. S2). The mixed-valence Mn (II/III)-bearing minerals in these grains were similar to braunite ($Mn_6^{III}Mn^{II}O_8SiO_4$) and Mn_3O_4 (Figs. 5B and S2), consistent with detrital silicates or with oxides that have undergone partial reduction in the anoxic basin. Lenz et al. (2014) determined that similar spectra obtained from euxinic Baltic Sea sediments represented Mn in aluminosilicates rather than Mn oxides, although we could not definitively distinguish between these phases in our samples. No manganese (IV) oxides were detected in the sediments and did not appear to have survived transit through the anoxic water column without partial or complete reduction.

Reductive dissolution of Mn(IV) oxides is expected to have occurred rapidly in the lower chemocline and euxinic monimolimnion due to high concentrations of sulfide and dissolved Fe^{2+} reductants (Myers and Nealson, 1988). Dissolved Mn^{2+} that was generated by reductive dissolution was available to form carbonate phases (Lee et al., 2011) or may have facilitated partial reduction of Mn(IV) to Mn(III) oxides (Bargar et al., 2005; Elzinga, 2011; Johnson et al., 2016a). Manganese (IV) oxides were likely limited to oxic surface waters where they were input from surface runoff or precipitated at the oxic-anoxic interface due to microbial oxidation of Mn^{2+} transported upward from the chemocline (Trefry et al., 1984; Van Cappellen et al., 1998; Clement et al., 2009). Particulate Mn (III/IV)-oxides subsequently settled back down into the chemocline where they could undergo reductive dissolution by microorganisms and continue to be cycled between oxic and anoxic waters (Van Cappellen et al., 1998).

4.2. Iron geochemistry

Acid-soluble Fe comprised 24–45% of total sediment Fe and was attributed to acid-volatile sulfides (e.g., Fe monosulfides) (Suits and Wilkin, 1998) since there was no evidence for siderite ($FeCO_3$) formation. Small amounts of acid-soluble Fe are known to dissolve from aluminosilicates or poorly crystalline iron oxides (Raiswell et al., 1994), although no poorly crystalline Fe oxides (e.g., ferrihydrite) were detected in these sediments. Rather, our evidence indicates that Fe was present in aluminosilicates and in sulfide minerals such as mackinawite (FeS), greigite (Fe_3S_4), and pyrite and marcasite (FeS_2). High concentrations of dissolved Fe in sediment pore waters (Fig. 3) and mineral overgrowth on a subset of iron sulfide framboids (Fig. 7) indicate that iron sulfides underwent diagenetic alteration in the sediments following nucleation in the water column (Wilkin and Barnes, 1997; Suits and Wilkin, 1998). The co-occurrence of greigite with mackinawite and pyrite also suggests mineral transformation in the sediments. Greigite is a metastable intermediate in the transformation of mackinawite to pyrite (Lennie and Vaughan, 1996; Hunger and Benning, 2007), and its formation is thermodynamically favored in the FGL water column (Havig et al., 2015) (Fig. S6). Greigite-containing framboids in the sediments (Fig. 7) reflect the morphology of framboids collected from the FGL water column (Suits and Wilkin, 1998) and elsewhere (Ariztegui and Dobson, 1996). Iron oxides can settle through the FGL water column and collect in the sediments with only partial reduction from iron (III) oxides to the mixed-valence ($Fe^{II}Fe^{III}$) magnetite; thus, it is possible that magnetite is also present. However, magnetite would not account for the presence of S or measured Fe:S stoichiometry in these grains.

We infer from the depth distribution of these different phases (Fig. 7) that FeS minerals were formed in the water column or in recently deposited sediments but transitioned to greigite and pyrite or marcasite with subsequent burial. These results are consistent with previous studies that demonstrate extensive pyrite formation during diagenesis in FGL sediments (Suits and Wilkin, 1998). No Fe spectra were consistent with iron carbonate, indicating that no appreciable siderite formation or Fe substitution into calcite occurred. Rather, in this sulfur-rich but Fe-limited system (Suits and Wilkin, 1998), Fe was exclusively preserved in an assemblage of iron sulfides that converge towards FeS_2 with increasing time and burial depth. The persistence of oxygen-sensitive iron sulfides in the sediments indicates that the basin has remained anoxic with no transient periods of oxygenation.

5. CONCLUSIONS

In this study, we demonstrate that Mn-bearing carbonates and assemblages of Fe and Mn sulfide minerals accumulate in sediments underlying a euxinic basin. Our results provide evidence that preservation of this mineral

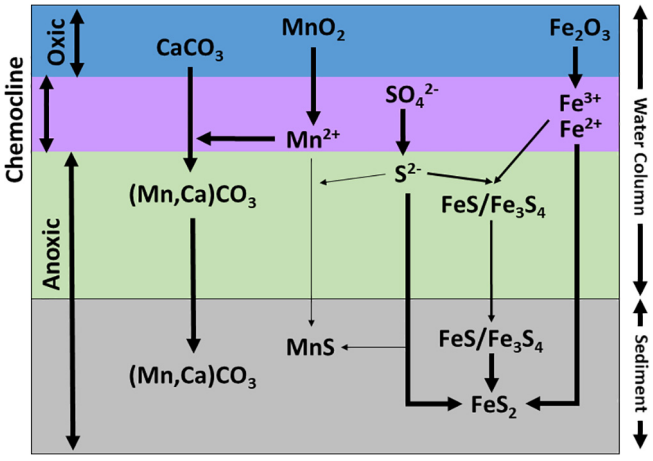

Fig. 8. Conceptual model of Mn and Fe transport through the water column and deposition into the sediments of Fayetteville Green Lake. Reduction of iron and manganese oxides occurs in the chemocline to generate high concentrations of dissolved species that are removed from the water column primarily through either precipitation on settling calcite grains (Mn) or reaction with dissolved sulfide (Fe). Manganese carbonates accumulate in sediments with minimal alteration whereas iron sulfides undergo diagenesis to FeS_2 phases (pyrite and marcasite). Manganese sulfides may also form in the water column and/or sediments.

assemblage in sediments reflects dynamic biogeochemical cycling in an overlying, stratified water column. A conceptual model for Mn and Fe cycling in the water column and sediments is presented in Fig. 8. While sulfide minerals both precipitate in the water column and undergo diagenesis in anoxic sediments, carbonates are exclusively formed in the water column and undergo minimal alteration following deposition. Manganese is largely associated with carbonates, although dissolved Mn that is not incorporated into carbonate phases may precipitate as sulfide minerals in close association with framboidal Fe sulfides. Authigenic Fe is not incorporated into carbonates but is exclusively preserved in sulfides that converge towards FeS_2 (pyrite and marcasite) with sediment depth. Further research is needed to characterize the geochemistry of particles that form in the stratified water column in order to elucidate mineralogical transformations that occur as grains settle through the chemocline and euxinic basin. These analyses would reveal the extent to which Mn is incorporated into calcite grains at various depths in the water column, as well as illustrate the formation and alteration of Fe and Mn-bearing sulfide phases that collect in sediments.

Our results challenge current understanding of how Mn is cycled in redox-stratified water bodies and preserved in sediments. Previously, manganese carbonates were thought to form primarily from the diagenetic alteration of manganese oxides deposited in surface sediments that were subsequently buried, reduced in anoxic sediments, and precipitated as authigenic manganoan carbonates (Calvert and Pedersen, 1996; Maynard, 2010; Johnson et al., 2013; Johnson et al., 2016b). Here, we suggest that manganoan carbonate phases can accumulate in sediments below euxinic bottom waters following precipitation on biogenic calcite in the oxygen-minimum zone of the water column. This proposed mechanism does not require reductive dissolution of Mn(IV) oxides to occur in the sediments. The implication of this finding is that the presence of manganoan carbonate does not necessarily denote the existence of oxygenated bottom waters. Rather, the manganese carbonates that characterize Proterozoic deposits may have accumulated below stratified water bodies with high concentrations of dissolved Mn in the chemocline and euxinic bottom waters. Future work is needed to test whether this mechanism is viable for generating manganoan carbonate ores under conditions that favor higher Mn accumulation in sediments, such as higher dissolved Mn concentrations or increased residence time of calcite grains in the Mn^{2+}-enriched zone of the water column.

ACKNOWLEDGEMENTS

This research used resources of the Advanced Photon Source, a DOE Office of Science User Facility operated by Argonne National Laboratory under Contract No. DE-AC02-06CH11357. We acknowledge the support of GeoSoilEnviroCARS (Sector 13), which is supported by NSF Earth Sciences (EAR-1128799), and DOE Geosciences (DE-FG02-94ER14466). Portions of this work were supported by NASA Astrobiology Institute Cooperative Agreement NNA09DA76A. The authors thank Elizabeth Swanner, Jena Johnson, Vincent Noël, and Thilo Behrends for contributing XANES reference spectra. We also thank Hamilton College students Thomas Blanchard, Jonah Boucher, Jenna Crawford, and Eric Nieminen for their assistance during sample collection and processing, the Hamilton College Dean of Faculty for providing student summer research stipends, and Bruce Wegter for operating the Hamilton College research vessel. Additionally, we thank the Green Lakes State Park staff and the New York State Department of Parks for providing access to Green Lake. The authors would also like to acknowledge the reviewers whose comments helped to improve and clarify this work.

APPENDIX A. SUPPLEMENTARY MATERIAL

Supplementary data associated with this article can be found, in the online version, at https://doi.org/10.1016/j.gca.2018.04.013.

REFERENCES

Ariztegui D. and Dobson J. (1996) Magnetic investigations of framboidal greigite formation: a record of anthropogenic environmental changes in eutrophic Lake St Moritz, Switzerland. *The Holocene* **6**, 235–241.

Arnold G. L., Anbar A. D., Barling J. and Lyons T. W. (2004) Molybdenum isotope evidence for widespread anoxia in mid-Proterozoic oceans. *Science* **304**, 87–90.

Bargar J. R., Tebo B. M., Bergmann U., Webb S. M., Glatzel P., Chiu V. Q. and Villalobos M. (2005) Biotic and abiotic products of Mn(II) oxidation by spores of the marine Bacillus sp. strain SG-1. *Am. Mineral.* **90**, 143–154.

Bekker A., Slack J. F., Planavsky N., Krapež B., Hofmann A., Konhauser K. O. and Rouxel O. J. (2010) Iron formation: the sedimentary product of a complex interplay among mantle, tectonic, oceanic, and biospheric processes. *Econ. Geol.* **105**, 467–508.

Bottcher M. E. (1998) Manganese(II) partitioning during experimental precipitation of rhodochrosite – calcite solid solutions from aqueous solutions. *Mar. Chem.* **62**, 287–297.

Bottcher M. E. and Huckriede H. (1997) First occurrence and stable isotope composition of authigenic γ-MnS in the central Gotland Deep (Baltic Sea). *Mar. Geol.* **137**, 201–205.

Calvert S. E. and Pedersen T. F. (1996) Sedimentary geochemistry of manganese: Implications for the environment of formation of manganiferous black shales. *Econ. Geol.* **91**, 36–47.

Clement B. G., Luther G. W. and Tebo B. M. (2009) Rapid, oxygen-dependent microbial Mn(II) oxidation kinetics at sub-micromolar oxygen concentrations in the Black Sea suboxic zone. *Geochim. Cosmochim. Acta* **73**, 1878–1889.

Cline J. D. (1969) Spectrophotometric determination of hydrogen sulfide in natural waters. *Limnol. Oceanogr.* **14**, 454–458.

Eggleton F. E. (1931) A limnological study of the profundal bottom fauna of certain fresh-water lakes. *Ecol. Monogr.* **1**, 232–331.

Elzinga E. J. (2011) Reductive transformation of birnessite by aqueous Mn(II). *Environ. Sci. Technol.* **45**, 6366–6372.

Franklin M. L. and Morse J. W. (1983) The interaction of manganese (II) with the surface of calcite in dilute solutions and seawater. *Mar. Chem.* **12**, 241–254.

Fry B. (1986) Sources of carbon and sulfur nutrition for consumers in three meromictic lakes of New York State. *Limnol. Oceanogr.* **31**, 79–88.

Havig J. R., Hamilton T. L., McCormick M., McClure B., Sowers T., Wegter B. and Kump L. R. (2017) Water column and sediment stable carbon isotope biogeochemistry of permanently redox-stratified Fayetteville Green Lake, New York, U.S.A. *Limnol. Oceanogr.* **63**, 570–587.

Havig J. R., McCormick M. L., Hamilton T. L. and Kump L. R. (2015) The behavior of biologically important trace elements across the oxic/euxinic transition of meromictic Fayetteville Green Lake, New York, USA. *Geochim. Cosmochim. Acta* **165**, 389–406.

Helz G. R., Bura-Nakić E., Mikac N. and Ciglenečki I. (2011) New model for molybdenum behavior in euxinic waters. *Chem. Geol.* **284**, 323–332.

Hilfinger, IV, M. F., Mullins H. T., Burnett A. and Kirby M. E. (2001) A 2500 year sediment record from Fayetteville Green Lake, New York: evidence for anthropogenic impacts and historic isotope shift. *J. Paleolimnol.* **26**, 293–305.

Huckriede H. and Meischner D. (1996) Origin and environment of manganese-rich sediments within black-shale basins. *Geochim. Cosmochim. Acta* **60**, 1399–1413.

Huerta-Diaz M. A. and Morse J. W. (1992) Pyritization of trace metals in anoxic marine sediments. *Geochim. Cosmochim. Acta* **56**, 2681–2702.

Hunger S. and Benning L. G. (2007) Greigite: a true intermediate on the polysulfide pathway to pyrite. *Geochem. Trans.* **8**, 1.

Jensen D. L., Boddum J. K., Tjell J. C. and Christensen T. H. (2002) The solubility of rhodochrosite (MnCO3) and siderite (FeCO3) in anaerobic aquatic environments. *Appl. Geochem.* **17**, 503–511.

Johnson J. E., Webb S. M., Thomas K., Ono S., Kirschvink J. L. and Fischer W. W. (2013) Manganese-oxidizing photosynthesis before the rise of cyanobacteria. *Proc. Natl. Acad. Sci.* **110**, 11238–11243.

Johnson J. E., Savalia P., Davis R., Kocar B. D., Webb S. M., Nealson K. H. and Fischer W. W. (2016a) Real-time manganese phase dynamics during biological and abiotic manganese oxide reduction. *Environ. Sci. Technol.* **50**(8), 4248–4258.

Johnson J. E., Webb S. M., Ma C. and Fischer W. W. (2016b) Manganese mineralogy and diagenesis in the sedimentary rock record. *Geochim. Cosmochim. Acta* **173**, 210–231.

Kiratli N. and Ergin M. (1996) Partitioning of heavy metals in surface Black Sea sediments. *Appl. Geochem.* **11**, 775–788.

Kraft S., Stümpel J., Becker P. and Kuetgens U. (1996) High resolution x-ray absorption spectroscopy with absolute energy calibration for the determination of absorption edge energies. *Rev. Sci. Instrum.* **67**, 681–687.

Kump L. R., Pavlov A. and Arthur M. A. (2005) Massive release of hydrogen sulfide to the surface ocean and atmosphere during intervals of oceanic anoxia. *Geology* **33**, 397–400.

Lee J. H., Kennedy D. W., Dohnalkova A., Moore D. A., Nachimuthu P., Reed S. B. and Fredrickson J. K. (2011) Manganese sulfide formation via concomitant microbial manganese oxide and thiosulfate reduction. *Environ. Microbiol.* **13**, 3275–3288.

Lennie A. R. and Vaughan D. J. (1996) Spectroscopic studies of iron sulfide formation and phase relations at low temperatures. *Miner. Spectrosc. A Tribut. Roger G. Burn* **5**, 117–131.

Lenz C., Behrends T., Jilbert T., Silveira M. and Slomp C. P. (2014) Redox-dependent changes in manganese speciation in Baltic Sea sediments from the Holocene Thermal Maximum: An EXAFS, XANES and LA-ICP-MS study. *Chem. Geol.* **370**, 49–57.

Manceau A., Marcus M. A. and Grangeon S. (2012) Determination of Mn valence states in mixed-valent manganates by XANES spectroscopy. *Am. Mineral.* **97**, 816–827.

Maynard J. B. (2010) The chemistry of manganese ores through time: A signal of increasing diversity of earth-surface environments. *Econ. Geol.* **105**, 535–552.

McCormick M. L., Banishki N., Powell S., Rumack A. and Garrett J. M. (2014) A low cost multi-level sampling device for synchronous aseptic collection of environmental water samples. *J. Microbiol. Methods* **105**, 51–53.

Meyer K. M. and Kump L. R. (2008) Oceanic euxinia in earth history: causes and consequences. *Annu. Rev. Earth Planet. Sci.* **36**, 251–288.

Morse J. W. and Luther G. W. (1999) Chemical influences on trace metal-sulfide interactions in anoxic sediments. *Geochim. Cosmochim. Acta* **63**, 3373–3378.

Mucci A. (1988) Manganese uptake during calcite precipitation from seawater: conditions leading to the formation of a pseudokutnahorite. *Geochim. Cosmochim. Acta* **52**, 1859–1868.

Mucci A. (2004) The behavior of mixed Ca-Mn carbonates in water and seawater: controls of manganese concentrations in marine porewaters. *Aquat. Geochem.* **10**, 139–169.

Myers C. R. and Nealson K. H. (1988) Bacterial manganese reduction and growth with manganese oxide as the sole electron acceptor. *Science* **240**, 1319–1321.

Newville M. (2013) Larch: an analysis package for XAFS and related spectroscopies. In Journal of Physics: Conference Series p. 12007.

Noël V., Marchand C., Juillot F., Ona-Nguema G., Viollier E., Marakovic G., Olivi L., Delbes L., Gelebart F. and Morin G. (2014) EXAFS analysis of iron cycling in mangrove sediments downstream a lateritized ultramafic watershed (Vavouto Bay, New Caledonia). *Geochim. Cosmochim. Acta* **136**, 211–228.

Pierrot D., Lewis E. and Wallace D. W. R. (2006) MS Excel program developed for CO2 system calculations. ORNL/CDIAC-105a., Oak Ridge, Tennessee.

Pingitore N. E., Eastman M. P., Sandidge M., Oden K. and Freiha B. (1988) The coprecipitation of manganese(II) with calcite: an experimental study. *Mar. Chem.* **25**, 107–120.

Planavsky N. J., Bekker A., Hofmann A., Owens J. D. and Lyons T. W. (2012) Sulfur record of rising and falling marine oxygen and sulfate levels during the Lomagundi event. *Proc. Natl. Acad. Sci.* **109**, 18300–18305.

Planavsky N. J., McGoldrick P., Scott C. T., Li C., Reinhard C. T., Kelly A. E., Chu X., Bekker A., Love G. D. and Lyons T. W. (2011) Widespread iron-rich conditions in the mid-Proterozoic ocean. *Nature* **477**, 448–451.

Poulton S. W. and Canfield D. E. (2011) Ferruginous conditions: a dominant feature of the ocean through Earth's history. *Elements* **7**, 107–112.

Prescher C. and Prakapenka V. B. (2015) DIOPTAS : a program for reduction of two-dimensional X-ray diffraction data and data exploration. *High Press. Res.* **7959**, 1–8.

Raiswell R., Canfield D. E. and Berner R. A. (1994) A comparison of iron extraction methods for the determination of degree of pyritisation and the recognition of iron-limited pyrite formation. *Chem. Geol.* **111**, 101–110.

Reinhard C. T., Planavsky N. J., Robbins L. J., Partin C. A., Gill B. C., Lalonde S. V., Bek-ker A., Konhauser K. O. and Lyons T. W. (2013) Proterozoic ocean redox and biogeochemical stasis. *Proc. Natl. Acad. Sci.* **110**, 5357–5362.

Rouxel O. J., Bekker A. and Edwards K. J. (2005) Iron isotope constraints on the Archean and Paleoproterozoic ocean redox state. *Science* **307**, 1088–1091.

Scott C., Lyons T. W., Bekker A., Shen Y., Poulton S. W., Chu X. and Anbar A. D. (2008) Tracing the stepwise oxygenation of the Proterozoic ocean. *Nature* **452**, 456–459.

Severmann S., Lyons T. W., Anbar A., McManus J. and Gordon G. (2008) Modern iron isotope perspective on the benthic iron shuttle and the redox evolution of ancient oceans. *Geology* **36**, 487–490.

Suess E. (1978) Mineral phases formed in anoxic sediments by microbial decomposition of organic matter. *Geochim. Cosmochim. Acta* **43**, 339–352.

Suits N. S. and Wilkin R. T. (1998) Pyrite formation in the water column and sediments of a meromictic lake. *Geology* **26**, 1099–1102.

Takahashi T., Broecker W., Li Y. H. and Thurber D. (1968) Chemical and isotopic balances for a meromictic lake. *Limnol. Oceanogr.* **13**, 272–292.

Thompson J. B. and Ferris F. G. (1990) Cyanobacterial precipitation of gypsum, calcite, and magnesite from natural alkaline lake water. *Geology* **18**, 995–998.

Thompson J. B., Schultze-Lam S., Beveridge T. J. and Des Marais D. J. (1997) Whiting events: Biogenic origin due to the photosynthetic activity of cyanobacterial picoplankton. *Limnol. Oceanogr.* **42**, 133–141.

Trefry J. H., Presley B. J., Keeney-Kennicutt W. L. and Trocine R. P. (1984) Distribution and chemistry of manganese, iron, and suspended particulates in Orca Basin. *Geo-Marine Lett.* **4**, 125–130.

Van Cappellen P., Viollier E., Roy Choudhury A., Clark L., Ingall E., Lowe K. and DiChristina T. (1998) Biogeochemical cycles of manganese and iron at the oxic-anoxic transition of a Stratified Marine Basin (Orca Basin, Gulf of Mexico). *Environ. Sci. Technol.* **32**(19), 2931–2939.

Wilkin R. T. and Barnes H. L. (1997) Pyrite formation in anoxic estuarine basin. *Am. J. Sci.* **297**, 620–650.

Associate editor: Timothy Lyons